ADVANCED MATERIALS TECHNOLOGIES
www.advmattechnol.de

Additive Nanomanufacturing of Multifunctional Materials and Patterned Structures: A Novel Laser-Based Dry Printing Process

*Zabihollah Ahmadi, Seungjong Lee, Raymond R. Unocic, Nima Shamsaei, and Masoud Mahjouri-Samani**

Direct printing of functional materials, structures, and devices on various platforms such as flexible to rigid substrates is of interest for applications ranging from electronics to energy and sensing to biomedical devices. Current additive manufacturing (AM) and printing processes are either limited by the available sources of functional materials or require to be in the form of precisely designed inks. Here, a novel laser-based additive nanomanufacturing (ANM) system capable of in situ and on-demand generations of nanoparticles that can serve as nanoscale building blocks for real-time sintering and dry printing a variety of multifunctional materials and patterns at atmospheric pressure and room temperature is reported. The ability to print different functional materials on various rigid and flexible platforms is shown. This nonequilibrium process involves pulsed laser ablation of targets and in situ formation of pure amorphous nanoparticles' stream that are guided through a nozzle onto the surface of the substrate, where they are sintered/crystallized in real-time. Further, the process–structure relationship of the printed materials from nanoscale to microscale is shown. This new ANM concept opens up an opportunity for printing advanced functional materials and devices on rigid and flexible substrates that can be employed both on the earth and in space.

1. Introduction

The manufacturing complexity, cost, and excessive wastage of the conventional device micro/nanomanufacturing processes as well as their incompatibility with stretchable and dissolvable substrates have resulted in considerable efforts for developing new advanced manufacturing methods to overcome these challenges.[1] Additive manufacturing (AM) processes, commonly known as 3D printing, have attracted enormous attention in various industries such as aerospace, medical, automotive, fashion, and the environment.[2–6] Typically, AM builds up geometrically complex parts at the macroscale by adding microsized layers of material from a sliced computer-aided design (CAD) file.[7–9] This single-step process allows the design of custom parts and reduction of fabrication time, cost, and material consumption compared to conventional manufacturing methods. The ability to fabricate complex structures and devices via AM and materials printing technologies has led to a paradigm shift in engineering design and product realization. However, the limited choice of functional precursors and versatile printing techniques in the current AM technology are among the major challenges that significantly limit their applications in printing hybrid structures and devices with complex functionalities, including electronics, optoelectronics, flexible and wearable sensors, and energy conversion and storage devices.[10–16]

Among the AM categories,[17] inkjet and aerosol jet printing offer the possibility of fabricating a few electronics and functional devices.[18] Inkjet printing (IJP) relies on the ejection of ink droplets from a nozzle onto the substrate, which can be either rigid or flexible.[19–22] Conductive, dielectric, and polymeric inks are the most common materials used in IJP. Typically, the inks used for this technique are formulated with viscosities on the order of 1–20 centipoise (cp). The aerosol jet printing (AJP) is a relatively new printing technique developed in recent years.[23,24] In this process, liquid inks are first atomized into small droplets of ≈1–5 μm in diameter, then transported to the printing head through a carrier gas. Compared to

Z. Ahmadi, Prof. M. Mahjouri-Samani
Electrical and Computer Engineering Department
Auburn University
Auburn, AL 36849, USA
E-mail: mahjouri@auburn.edu

S. Lee, Prof. N. Shamsaei
Department of Mechanical Engineering
Auburn University
Auburn, AL 36849, USA

S. Lee, Prof. N. Shamsaei, Prof. M. Mahjouri-Samani
National Center for Additive Manufacturing Excellence (NCAME)
Auburn University
Auburn, AL 36849, USA

Dr. R. R. Unocic
Center for Nanophase Materials Sciences
Oak Ridge National Laboratory
Oak Ridge, TN 37831, USA

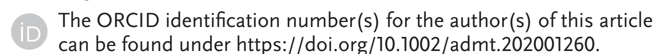
The ORCID identification number(s) for the author(s) of this article can be found under https://doi.org/10.1002/admt.202001260.

DOI: 10.1002/admt.202001260

 © 2021 Wiley-VCH GmbH

IJP, AJP is compatible with a wide range of materials, including high-viscosity inorganic inks, organics, and high aspect-ratio carbon nanotube (CNT) solutions.[25] In AJP, the sheath gas (usually nitrogen) in the print head prevents the nozzle from clogging and keeps the aerosol beam tightly focused.

In both systems, the use of solvents and surfactants/additives makes the inks impure and complex to handle. As a result, solvents removal and post thermal annealing make the device manufacturing process complicated and expensive.[26] In addition, the printed material should be in a viscous fluid state, making it difficult to obtain materials with the appropriate viscosities. The development of new source materials for IJP and AJP has become a priority for many researchers in order to enable the printing of functional devices. Determining optimal print parameters of ink is often a sensitive process. In addition, optimal printing parameters for a given ink do not, in general, translate to new materials, demanding an extensive, empirical optimization over a broad phase space for each additional ink or material. Therefore, printing multifunctional materials (e.g., ferromagnetic, piezoelectric) and hybrid structures is still a major challenge.[17,26–35] Direct printing of multifunctional materials and composites such as titanium dioxdie (TiO_2),[36–42] barium titanate (BTO),[43–45] indium tin oxide (ITO)[11,46] opens a new pathway toward the direct manufacturing of devices with complex functionality. This has led to the emergence of laser-based additive nanomanufacturing (ANM) as a promising approach that could enable the synthesis and patterning of a variety of materials with micro/nanoscale resolutions.[47–55]

Here, for the first time, we successfully introduced a single step ANM approach that enables the dry printing of a variety of multifunctional materials such as TiO_2, BTO, and ITO on different substrates using a laser source. Our novel printing method is based on the in situ and on-demand generation of metastable nanoparticles via the nonequilibrium pulsed laser ablation process that can be laser sintered/crystallized in real-time to form desired patterns and devices. Our novel laser-based ANM process possesses the capability to print a wide range of dry, contaminations-free, and intrinsically pure nanoparticles at room temperature and at atmospheric pressure. This approach also offers the flexibility of printing onto different types of substrates, including metals, ceramics, plastics, paper, and flexible substrates such as polydimethylsiloxane (PDMS) and polyethylene terephthalate (PET).

2. Experimental Section

2.1. Experimental Setup

Figure 1 shows the schematic of the designed and developed ANM apparatus. The system consisted of a pulsed excimer

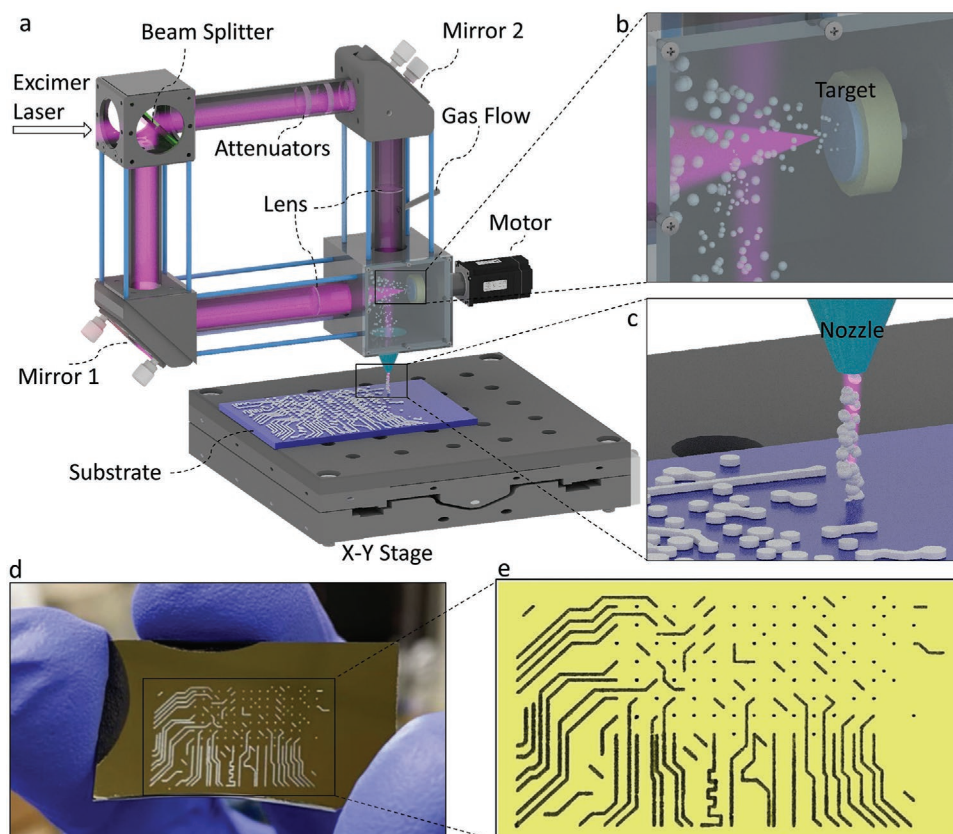

Figure 1. a) Schematic illustration of the ANM process used for printing various functional materials on the different substrates. b) Enlarged illustration of in situ and on-demand generating of nanoparticles by pulsed laser ablation of the desired target materials in atmospheric pressure and room temperature. c) Enlarged illustration of real-time laser sintering and crystallization of nanoparticles on the surface of the substrate. d) Optical image of printed ITO circuit lines using the ANM process. e) Enlarged optical image of the printed circuit lines.

© 2021 Wiley-VCH GmbH

laser (KrF, wavelength 248 nm), a beam splitter, two adjustable turning mirrors, two lenses with 150 mm focal length, an ablation chamber with a nozzle, a target and its holder, an X–Y computer-controlled positioning system, attenuators, and controlled Ar/N_2 gas connected to the cylindrical holder by a feeder pipe. A substrate was placed onto the X–Y motion table. The separation between the nozzle and the substrate was kept constant at 0.5 mm. All the components were placed on an optical table.

The ANM fabrication process involved five key steps, as shown in Figure 1a, as listed in this paragraph. 1) *Splitting pulsed excimer laser beam*: the 248 nm excimer laser beam was divided into ablation and sintering/crystallization beams by a beam splitter (70% reflection, 30% transmission), and then the two beam energies were further tuned and guided toward mirrors 1 and 2, respectively. 2) *Pure amorphous nanoparticles generation*: the ablation laser beam was directed toward a sealed environmental chamber using mirror 1. The ablation laser beam was then focused onto the surface of the target by a ultraviolet (UV) fused silica convex lens to generate pure amorphous nanoparticles. The target was rotated by a step motor at an angular speed of ≈3 rad s^{-1} to avoid laser piercing. During the interaction of the ablation laser beam with the target, a laser-plasma plume was formed. The interaction of this plume with the background gas resulted in thermalization and condensation of the plume leading to the formation of nanoparticles.

Figure 2 shows the scanning electron microscopy (SEM) and scanning transmission electron microscopy (STEM) images of the laser-generated amorphous TiO_2 (a-TiO_2) nanoparticles with a size distribution of around 3–7 nm. 3) *Nanoparticles delivery*: a stream of produced pure amorphous nanoparticles was delivered to a central point beneath the nozzle head using a carrier gas flow. 4) *Sintering/crystallization of produced pure amorphous nanoparticles*: the sintering/crystallization laser beam was focused above the surface of the substrate using mirror 2 and a convex lens (see the Supporting Information). The nanoparticles were then sintered and crystallized on the surface of the substrate. Optical attenuators were used inside cylindrical holders to attenuate and tune the energy of ablation and sintering/crystallization laser beam, i.e., to reduce optical power. 5) *Stage scanning*: the substrate placed on an X–Y stage, which was computer programmed to move and form any predefined patterns. The operation principle of the system was similar to the laser beam directed energy deposition (LB-DED) processes;[9,56,57] however, the major difference here was the in situ and on-demand formation of nanoscale building blocks.

It should be noted that although an excimer laser was used in this work, other lasers might be employed. Regarding the ablation and nanoparticle formation process, any type of pulsed lasers that could meet the desired materials' ablation threshold could be used in this ANM process. In general, shorter wavelengths (higher photon energy) and shorter pulse widths (high peak power) were the two key parameters for efficient ablation of a wide range of solid targets. Therefore, any lasers that could meet such specifications could be used in the ablation process. Also, depending on what materials and what type of substrates were involved in the process, various sintering beams could be employed. Here, UV laser was used due to shallow depth of absorption to slightly sinter the nanoparticles without damaging the underlying substrate. However, if the substrates were more tolerant to heat, other types of lasers could be used for the sintering process.

2.2. Experimental Procedure

Solid targets (TiO_2, BTO, ITO) with 99.9% purity were used for laser ablation and formation of nanoparticles. Different nozzles with hole diameters of ≈100, 200, and 300 µm were used for the deposition (see the Supporting Information). For the first set of experiments, TiO_2 was selected as the test target. Various laser fluences ranging from 1.9 to 2.3 J cm^{-2} and 0.074 to 0.74 J cm^{-2} were used for the ablation of the target and sintering/crystallization of produced pure amorphous nanoparticles, respectively. Moreover, different repetition rates, including 5, 10, 15, and 20 Hz were used for the ablating and sintering processes. Various gas flow rates ranging from ≈1 to 4.58 SLPM (standard liter per minute) were used to regulate the flow of nanoparticles out of the nozzle. A set of comprehensive experiments were performed to understand the effect of process parameters (e.g., energy, frequency, gas flow rate, ablation and sintering time, and deposition overlap) on the printed materials.

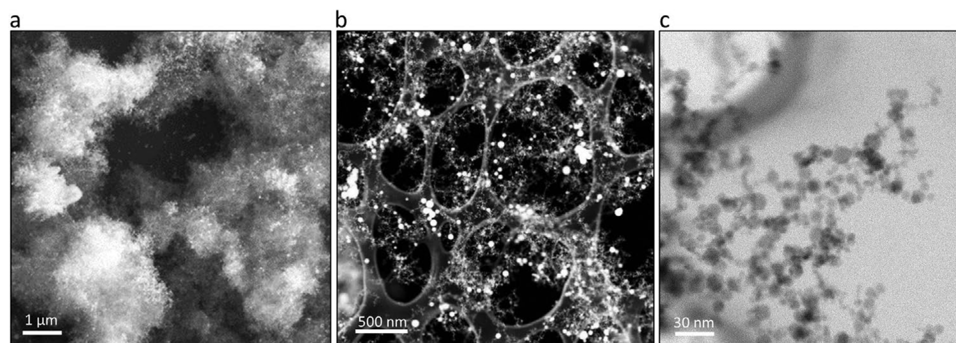

Figure 2. a) SEM image of ablated pure amorphous TiO_2 nanoparticles. b) STEM and c) High-angle annular dark-field (HAADF) images with different magnifications of ablated pure amorphous TiO_2 nanoparticles.

© 2021 Wiley-VCH GmbH

3. Results and Discussion

3.1. Formation of Nanoparticle Building Blocks

One of the key steps in this ANM process is the in situ and on-demand formation of stoichiometric nanoparticles by condensation of laser-generated plasmas plume at room temperature and atmospheric pressure. These nanoparticles serve as the building blocks that can be sintered and crystallized in real-time during the printing process. To investigate the size and structures of these nanoparticles, we performed atomic imaging measurements. Figure 2 shows the SEM and STEM images of the as-deposited TiO_2 nanoparticles (ablation energy (AE) = 2.3 J cm^{-2}, gas flow rate (GFR) = 2.8 SLPM, sintering/crystallization energy (S/C E) = blocked, repetition rate (RR) = 10 Hz). The as-deposited nanoparticles form an ensemble of a fluffy and porous deposition as shown by the SEM image in Figure 2a. These nanoparticles are mostly amorphous with a size distribution of about 3–7 nm in diameter, as shown by the STEM images in Figure 2b,c. The ability to generate such nanoparticle building blocks enables nanoscale precision in controlling the composition and thickness of the printed lines and allows simple integration and sintering into larger crystalline structures.

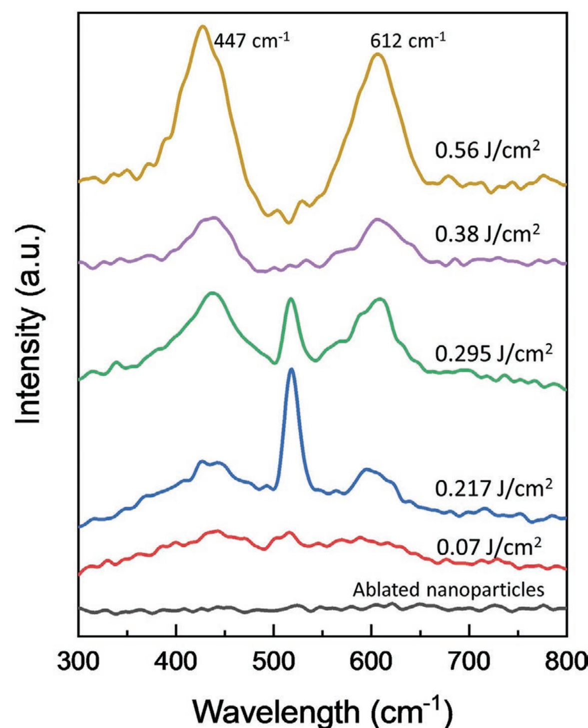

Figure 3. Representative Raman spectra of TiO_2 nanoparticles sintered at different crystallization energies, 0.07 up to 0.56 J cm^{-2}.

3.2. Sintering, Crystallization, and Printing Processes

The interaction of the sintering/crystallization laser beam with in situ generated TiO_2 nanoparticles at the surface of the substrate led to the formation of crystalline rutile TiO_2. To investigate the effect of the laser beam energy on the crystallization and sintering of amorphous TiO_2 nanoparticles, various samples were prepared and studied by Raman spectroscopy, as shown in **Figure 3**. Examining the Raman data from the in situ generated pure amorphous nanoparticles (while sintering/crystallization beam was blocked) showed a broad spectrum with no explicit peaks suggesting that the generated TiO_2 nanoparticles are primarily a-TiO_2. In addition, by increasing the crystallization energy (0.07–0.56 J cm^{-2}) while other parameters (AE = 2.3 J cm^{-2}, RR = 10 Hz, GFR = 2.8 SLPM, time = 30 s) kept constant, the in situ generated a-TiO_2 nanoparticles started to sinter and crystallize on the surface of the Si/SiO_2 substrates. The explicit threshold of crystallization was observed by the appearance of several new Raman peaks when crystallization energy was around 0.217 J cm^{-2} as shown in Figure 3. The Raman lines at 447 cm^{-1} and 612 cm^{-1} are assigned to the E_g, A_{1g} modes of the rutile TiO_2 phase, respectively.[58] The peak at 521 cm^{-1} is assigned to the Si/SiO_2 substrate Raman vibration mode. The intensity of the E_g and A_{1g} modes increases by increasing the sintering/crystallization laser fluence from 0.217 to 0.56 J cm^{-2}. The intensity of the Raman peaks is directly proportional to the crystallization quality and the thickness of the printed TiO_2.[59] It should be noted that increasing the sintering laser fluence beyond a certain threshold can re-ablate the printed layers from the substrate (≈1 J cm^{-2} for TiO_2). It is also worth mentioning that, depending on the substrate material, the energy of the sintering/crystallization beam may not be increased beyond the damage threshold of the substrate at the start of the deposition.

Morphologies of the printed TiO_2 layers on the Si/SiO_2 substrates at various process conditions were investigated by SEM, as shown in **Figure 4**. By turning off the sintering/crystallization beam, the printed nanoparticles were mainly agglomerates of amorphous TiO_2 nanoparticles (AE = 2.3 J cm^{-2}, GFR = 1.9 SLPM, RR = 10 Hz), as seen in Figure 4a and also confirmed by the STEM images in Figure 2. The SEM images shown in Figure 4b–h confirmed that during laser sintering/crystallization, the nanoparticles fused together to form larger crystalline rutile TiO_2 structures. As depicted in Figure 4b–d, the feature size, as well as the thickness of the printed crystalline TiO_2 nanostructure, were continuously increased by increasing the time from 60 to 270 s, while keeping all the other processing parameters constant (AE = 2.3 J cm^{-2}, GFR = 2.8 SLPM, S/C E = 0.3 J cm^{-2}, RR = 10 Hz). At longer deposition times, more TiO_2 nanoparticles were generated and delivered to the nozzle, resulting in thicker deposited layers. Other samples with different sintering/crystallization energies (0.295, 0.4, 0.67 J cm^{-2}), while keeping all the other processing parameters constant (AE = 2.3 J cm^{-2}, GFR = 2.8 SLPM, time = 60 s, RR = 10 Hz), were also investigated, and corresponding results are shown in Figure 4f–h. Accordingly, the density, thickness, and feature sizes of the printed TiO_2 layers were increased at higher sintering/crystallization energies, which was in agreement with the results observed from the Raman spectra shown in Figure 3.

© 2021 Wiley-VCH GmbH

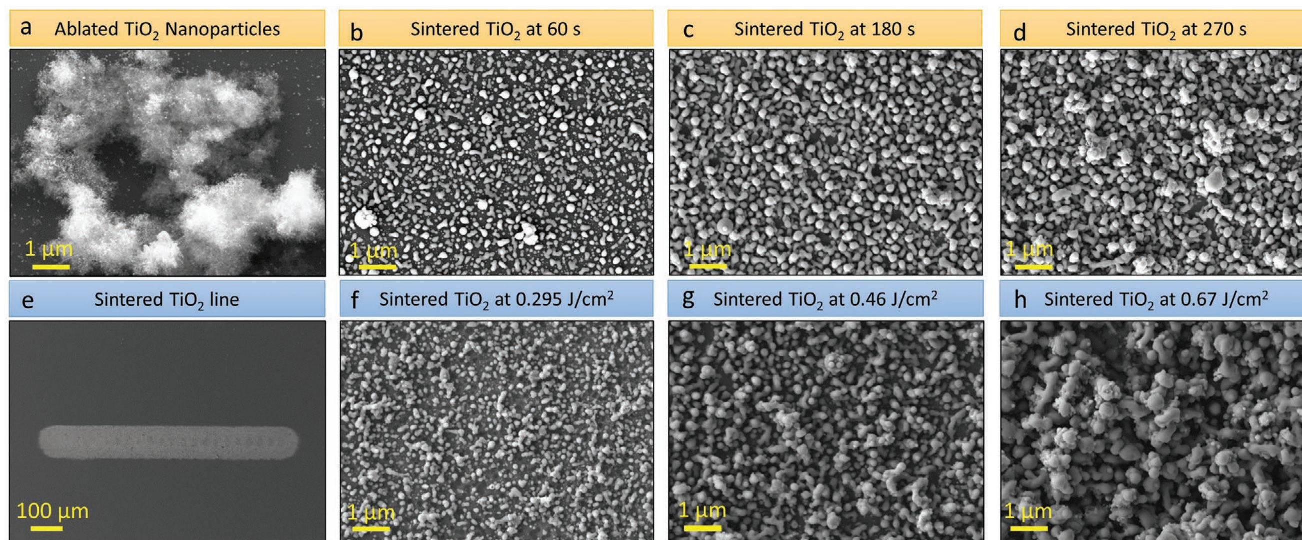

Figure 4. a) SEM image of as-produced amorphous TiO_2 ablated by laser, sintered TiO_2 at b) 60 s, c) 180 s, and d) 270 s while crystallization energy and other parameters are kept constant. e) Line created by ANM method (ablation energy = 2.3 J cm^{-2}, gas flow rate = 2.8 SLPM, sintering/crystallization energy = 0.3 J cm^{-2}, repetition rate = 10 Hz, 90% overlap, X–Y delay = 5 s) with 100 µm nozzle diameter, sintered TiO_2 at f) 0.295 J cm^{-2}, g) 0.4 J cm^{-2}, h) 0.67 J cm^{-2} crystallization energy while time (60 s) and other parameters are kept constant.

3.3. Factors Affecting Printing Efficiency

3.3.1. Influence of Gas Flow and Laser Repetition Rates

Understanding the role of process parameters is important in this ANM process as they govern the amount of nanoparticles that are generated, delivered, sintered to form crystalline printed layers and patterns. For a given ablation energy (2.3 J cm^{-2}), deposition time (60 s), and target material (TiO_2), the thickness variation of printed TiO_2 crystalline layers on the Si/SiO_2 substrate was analyzed, as a function of gas flow and laser repetition rates, as shown in **Figure 5**. The red and

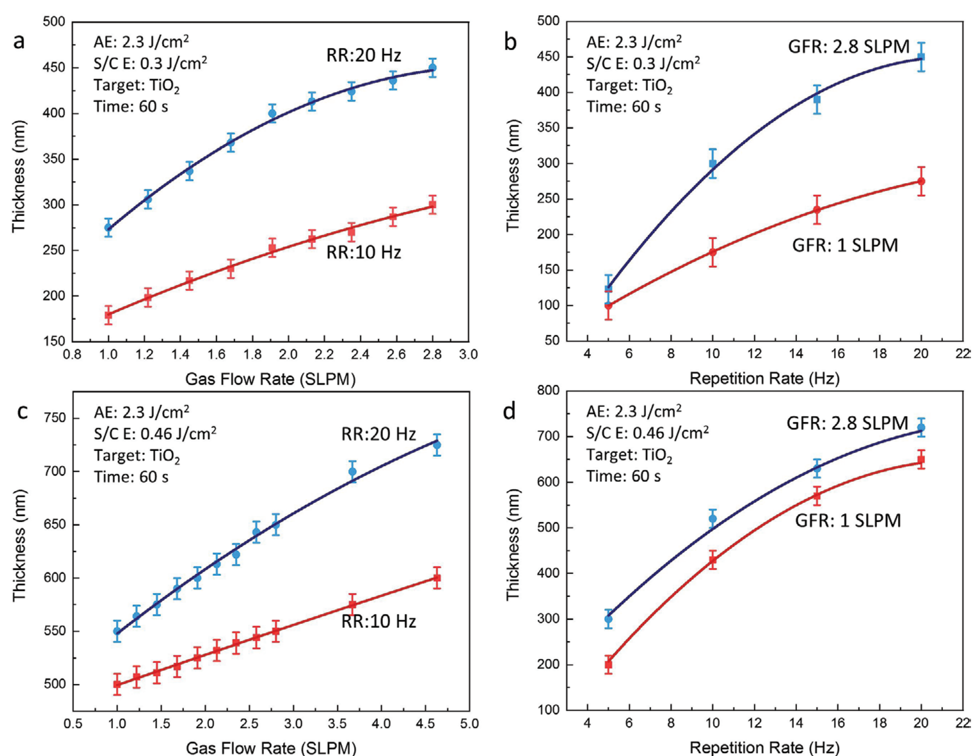

Figure 5. The thickness of ANM-printed dots as a function of gas flow rate for a) 0.3 J cm^{-2} and c) 0.46 J cm^{-2} in sintering/crystallization energies. The thickness of ANM-printed dots as a function of repetition rate with b) 0.3 J cm^{-2} and d) 0.46 J cm^{-2} in sintering/crystallization energies.

© 2021 Wiley-VCH GmbH

navy blue curves in Figure 5a show the thickness versus gas flow rate while the repetition rate is 10 and 20 Hz, respectively. When GFR changed from 1 to 2.8 SLPM, as it is illustrated in Figure 5a, the thickness increased from ≈175 to ≈300 nm (in 10 Hz, red curve) and ≈275 to ≈450 nm (in 20 Hz, navy blue curve), suggesting that increased gas flow rate would result in increased deposition thicknesses. In Figure 5b (red curve), when the repetition rate changed from 5 to 20 Hz, the thickness of printed TiO_2 crystalline layers increased from ≈100 to ≈275 nm. By changing the gas flow rate to 2.8 SLPM, Figure 5b (navy blue curve), while the repetition rate changed from 5 to 20 Hz, the thickness increased from ≈125 to ≈450 nm, suggesting that increased repetition rate would result in increased deposition thicknesses. Moreover, the same measurements were performed while the crystallization energy changed to 0.46 J cm^{-2}, as shown in Figure 5c,d. A significant change in the thickness was observed compared to Figure 5a,b. It can be concluded that at lower sintering/crystallization laser energies, some of the amorphous nanoparticles coming out of the nozzle might rebound away from the surface before they have a chance to get sintered onto the printed lines. Higher sintering/crystallization laser energies tightly sinter the incoming nanoparticles on the substrate, and consequently, the thickness of the printed line increases. However, one should avoid excessive energies beyond the re-ablation threshold, as mentioned above. These results show that both gas flow and repetition rates have a significant effect on the deposition thicknesses. Moreover, when the sintering/crystallization laser was blocked, due to the continuity of gas flow, most of the nanoparticles did not adhere well to the substrate and could be blown away from the surface.

3.3.2. *Influence of Deposition Time and Printing Overlap*

Figure 6a shows the thickness of crystallized and sintered TiO_2 nanoparticles deposited on the SiO_2 substrate as a function of time. The thickness increases from ≈250 to ≈550 nm as the time increases from 10 to 60 s (green curve, 1 SLPM). The changing trend of the thickness with time is the same for higher GFR, red and blue curves, implying that the thickness is also governed by time. Figure 6b,c shows the effect of deposition overlap (OL) on the thickness of deposited TiO_2 nanoparticles. Generally, increasing overlap via decreasing the stage velocity will result in the increment of the thickness. Three different overlaps numbers of 0%, 50%, and 75% were tested by the ANM system, while all other parameters were kept the same (AE = 2.3 J cm^{-2}, S/C E = 0.38 J cm^{-2}, GFR = 1.9 SLPM, RR = 10 Hz). The thickness measurement results showed an increment of thickness from ≈200 nm (for 0% overlap) to ≈600 nm (for 75% overlap).

According to the experimental results, we observed that larger diameter (>400 µm) nozzles would significantly disperse the nanoparticles, thus lowering the nanoparticles′ confinement efficiency during the printing process (see the Supporting Information). There was no evidence of noticeable deposition and sintering of TiO_2 on the substrate until the gas flow rate was set to more than 7.9 SLPM. However, the deposition/sintering area (circle with a diameter around ≈250 µm) is still significantly smaller than the size of the nozzle, showing a low deposition rate at a larger diameter of the nozzle, while printed patterns with 100–200 µm diameter nozzles have the same size as the nozzle.

3.4. Design and Printing of Various Patterns

The remarkable ability of our novel ANM system enables the realization of any arbitrary patterns of sintered nanoparticles on the substrates. This can be simply realized by the programmable motion of the X–Y stage during the printing process. As shown in **Figure 7**a–e, we have demonstrated the printing of different shapes and patterns on Si/SiO_2 substrates. Experiment parameters are provided in **Table 1**. The nozzle diameter size was 100 µm for all experiments. The different line widths

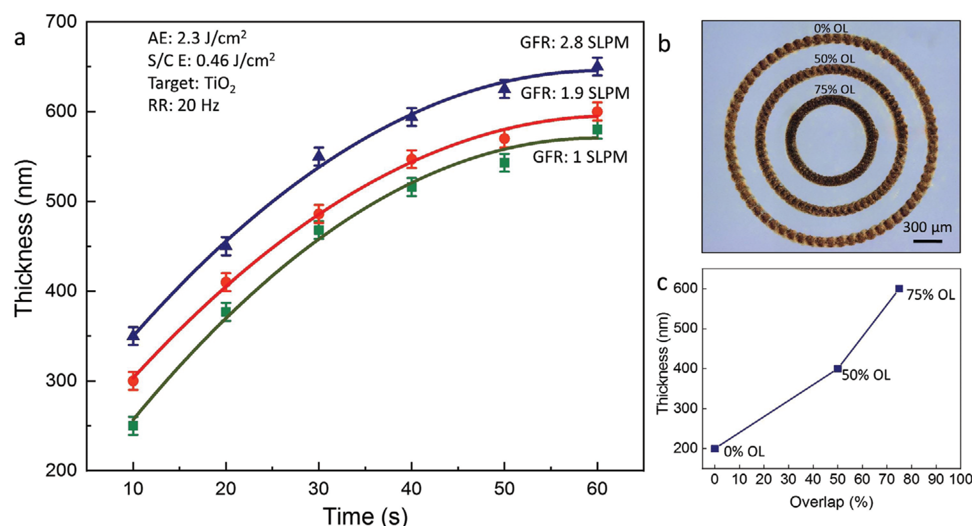

Figure 6. a) Sintered/crystallized TiO_2 thickness versus sintering time at ablation energy = 2.3 J cm^{-2}, sintering/crystallization energy = 0.46 J cm^{-2}, repetition rate = 20 Hz, and different values of gas flow rate. b) Optical images of ANM-printed circles with different overlap ratio. c) Sintered/crystallized TiO_2 thickness versus overlap.

© 2021 Wiley-VCH GmbH

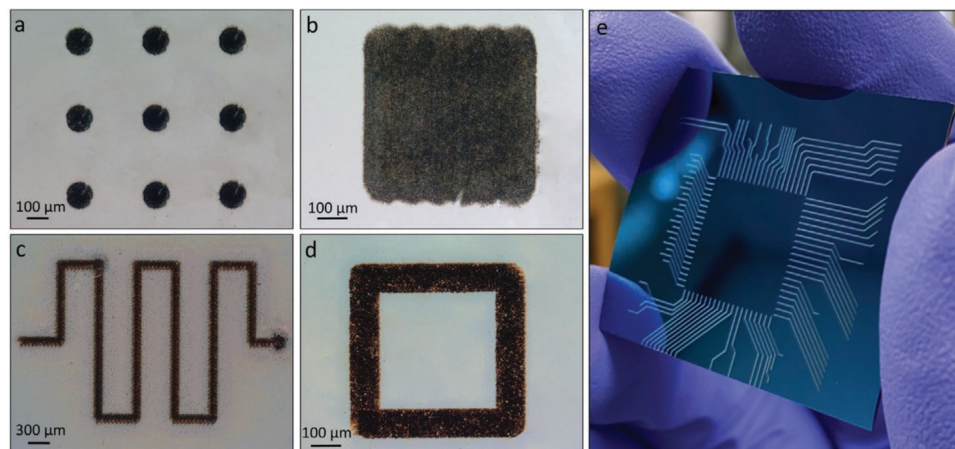

Figure 7. Optical images of a–d) printed TiO_2 and e) ITO patterns on SiO_2 substrate by ANM method.

will be achieved by changing the diameter size of the nozzle. These experiments clearly showed the promising flexibility and adaptability of the ANM process for dry and vacuum-free printing of various materials and patterns.

3.5. Printing Compatibility with Different Type of Materials and Substrates

To show the ANM's capability for printing other material systems, BTO and ITO patterns were also printed by this process. **Figure 8**a,d shows the SEM images of ablated ITO (AE = 2.3 J cm^{-2}) and BTO (AE = 2.3 J cm^{-2}) nanoparticles, respectively. Based on the STEM images shown in Figure 8b,e, the size of the as-synthesized nanoparticles was in the range of 3–7 nm. Similarly, these nanoparticle building blocks could be laser sintered and crystallized to form desired patterns. Figure 8c,f shows the sintered ITO (AE = 2.3 J cm^{-2}, S/C E = 0.23 J cm^{-2}, GFR = 2.8 SLPM, RR = 10 Hz) and BTO (AE = 2.3 J cm^{-2}, S/C E = 0.15 J cm^{-2}, GFR = 2.8 SLPM, RR = 10 Hz) nanoparticles in the ANM method, respectively. As illustrated in Figure 8c,f, the approximate diameter of the sintered/crystallized ITO and BTO crystal structures became between ≈50 and ≈250 nm. Cross-sectional SEM images of the printed ITO lines confirm the sintering of the ablated nanoparticles on SiO_2 substrate (see the Supporting Information). The proposed ANM system allows for printing various multifunctional materials for the fabrication of functional devices for sensing and energy applications. For instance, BTO is an important functional material in the electronics industry because of its superior dielectric, ferroelectric, piezoelectric, pyroelectric, and electro-optical properties. Using these characteristics, BTO films may find applications in ion sensors, biosensors, and pH sensors. ITO is a key transparent conductive oxide, and its most prominent applications are in transparent electrodes in liquid-crystal displays, organic light-emitting diodes, and touch-responsive screens, which can be found in smartphones and flat panel monitors. However, it is also used in applications such as low-emissivity windows, optoelectronic devices, solar cells, electrochromic windows, plasmonics, and lab-on-a-chip biosensing.

One of the fascinating advantages of this ANM process is it's suitability for printing on numerous substrates, including flexible substrates, paper, metals, glass, and ceramics. This is because of the dry printing and precision laser sintering nature of the ANM process. Hence, no liquid, polymer, or other binders are used in this system, and no postprocessing steps are required after the printing process. This enables applications in a variety of fields, including biosensing, photonics, storage, and sensing.[60–62] **Figure 9** shows printed ITO patterns onto different substrates, including copper, alumina oxide (Al_2O_3), PDMS, and paper (AE = 2.3 J cm^{-2}, S/C E = 0.39 J cm^{-2}, GFR = 2.8 SLPM, RR = 10 Hz, used for all). It should be noted that the high photon energy and low interaction time of our laser crystallizing process result in the nanoscale absorption and limited thermal penetration depth in the materials. This allows us to tune the crystallization within the nanoscale region of the nanoparticle coatings and hence avoid any damage to the underlying substrates. This study will be further extended in future in order to understand the interaction of the sintered nanoparticles with various substrates and reveal their process–structure–property relationships.

ITO lines with variable resistance values were successfully printed by real-time resistance monitoring during the printing

Table 1. Experimental parameters used for printing patterns of Figure 7.

Sample	AE [J cm^{-2}]	S/C E [J cm^{-2}]	Time [s]	GFR [SLPM]	RR [Hz]	OL [%]
a	2.3	0.46	60	2.8	20	0
b	2	0.54	5	1.9	10	90
c,d	1.7	0.3	5	2.8	10	90
e	2	0.25	5	2.8	10	90

© 2021 Wiley-VCH GmbH

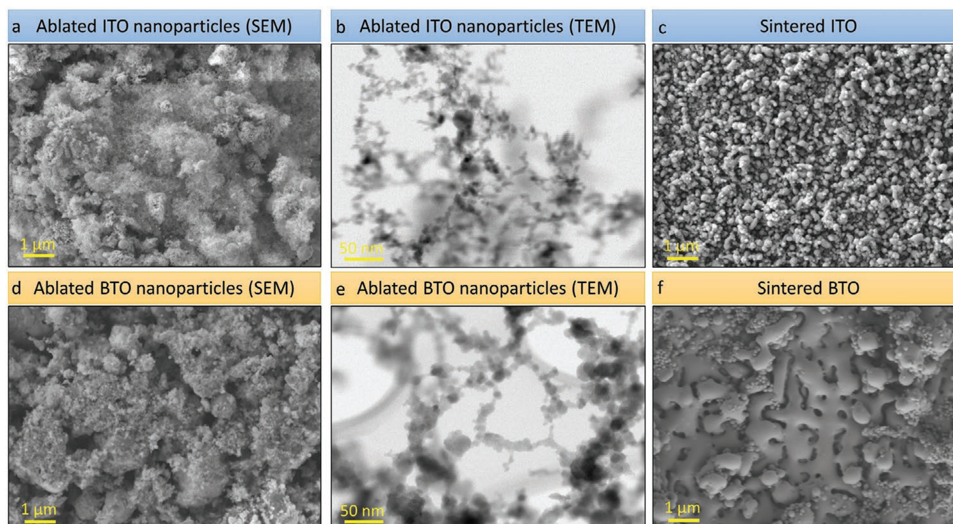

Figure 8. SEM images of ablated a) ITO and d) BTO nanoparticles. STEM images of ablated b) ITO and e) BTO nanoparticles. The SEM images of sintered and crystallized c) ITO and f) BTO.

process, as demonstrated in **Figure 10**. The resistance that can be controlled over a large range from 1 kΩ to 10 MΩ is ideally suited for low cost flexible electronic circuits. The resistance of printed lines was altered by repeating the printed path (number of the printed layers) to increase the thickness, while the length and width of the printed resistor line remained unchanged. Figure 10a shows the schematic diagram of the printing process and real-time resistance measurement. First, two ITO contacts were fabricated on PET substrate. By connecting two contacts to a digital multimeter, the resistance of the line was obtained in real-time during the printing process. As shown in Figure 10b–e, the number of printed paths, or equivalently the thickness of the printed ITO line, affected its resistance. More number of printed paths resulted in lower resistances, while less number of printed paths resulted in higher resistances. In addition, the printing process parameters such as repetition rate and sintering/crystallization energy also affected the resistance versus the number of printed path relationships, as shown in Figure 10b–d.

4. Conclusion

In summary, this paper reports the first demonstration of a novel laser-based additive nanomanufacturing method that enables the printing of various functional materials on different substrates. This new method allows the in situ and on-demand formation of various nanoparticle building blocks in atmospheric pressure and at room temperature. These nanoparticle building blocks can be directed toward the substrate through a nozzle forming a stream of nanoparticles that can be laser sintered/crystallized on various substrates in real-time. A set of comprehensive experimental studies were performed to decipher the effects of process parameters (gas flow rate, time, overlap, sintering energy, frequency repetition rate, thickness) of this ANM process on the printed materials and structures. Scanning electron microscopy and transmission electron microscopy were used for grain size confirmation. This method inherits the merits of producing nanoparticles that are dry, solution-free, and intrinsically pure that can be simultaneously laser sintered and crystallized to form contamination-free multifunctional materials prints on various rigid and flexible platforms such as PDMS, Si/SiO_2, paper, and ceramics. This method enables the future additive nanomanufacturing of hybrid multifunctional material and structures and print devices with complex functionalities.

5. Methods

Raman Spectra Measurement: A custom-made Raman system was used for optical diagnostics of TiO_2 and BTO crystallized by ANM system. The measurements were performed in a confocal microconfiguration using

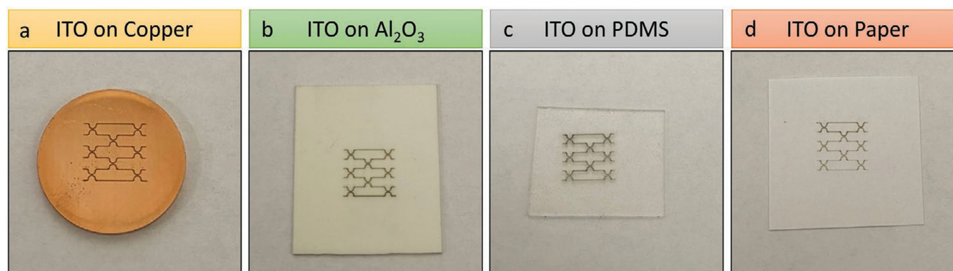

Figure 9. Photographic images of ITO patterns (200 µm line width) printed on a) copper, b) Al_2O_3, c) PDMS, and d) paper.

© 2021 Wiley-VCH GmbH

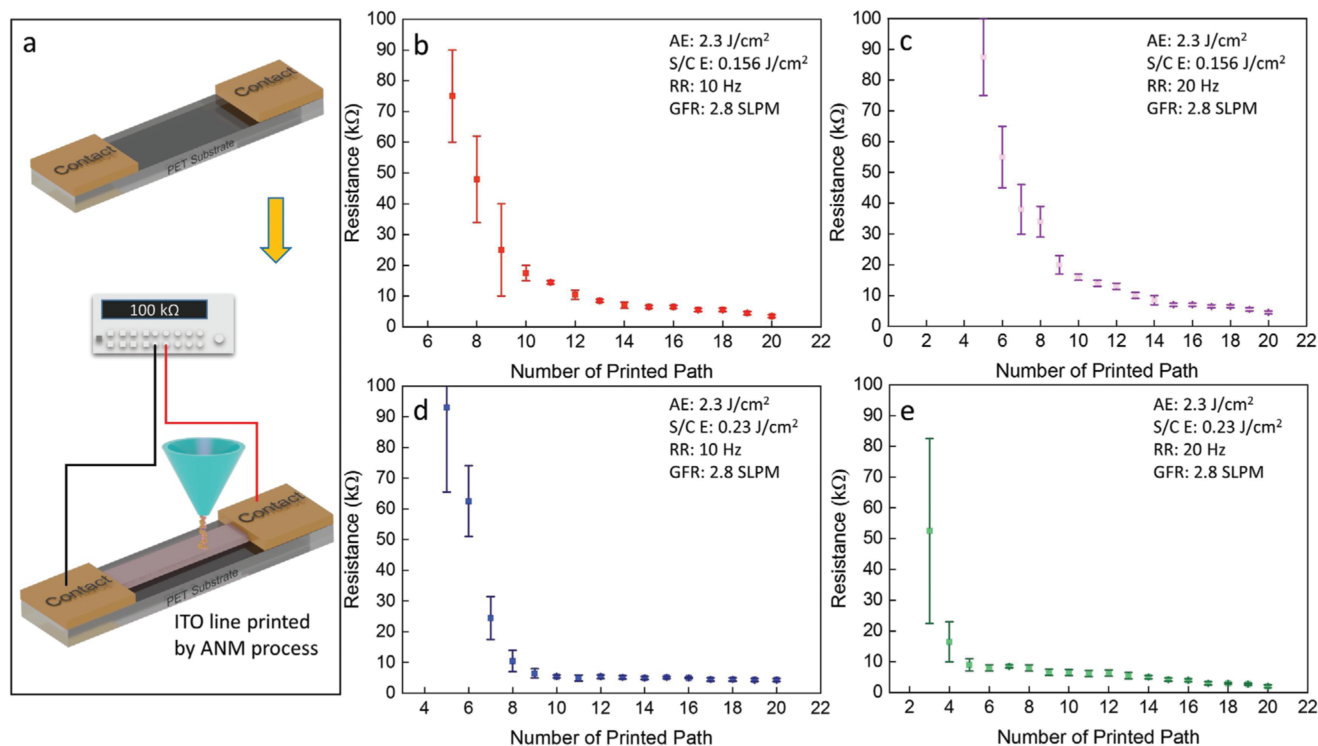

Figure 10. a) Real-time electrical resistivity measurement of 3 mm long lines while being printed by the ANM process as a function of the number of printed paths. Schematic illustration of deposited ITO line between two contact pads on a flexible PET substrate while the resistance is measured in real-time via a connected multimeter to pads. b) S/C E = 0.156 J cm^{-2}, RR = 10 Hz; c) S/C E = 0.156 J cm^{-2}, RR = 20 Hz; e) S/C E = 0.23 J cm^{-2}, RR = 10 Hz; d) S/C E = 0.23 J cm^{-2}, RR = 20 Hz.

a 50× microscope objective lens (NA = 0.9). A Horiba HR spectrometer was used with a 1200 grooves mm^{-1} grating and a laser excitation wavelength of 532 nm.

Scanning Electron Microscopy (SEM): The SEM images were obtained using Zeiss Crossbeam 550 microscope. The voltage and current were 5 KV and 2 nA, respectively.

STEM: STEM imaging was performed using a C_s corrected JEOL NeoARM operating at 80kV. Nanoparticles were directly deposited onto the TEM grid by holding the TEM grids under the printer nozzle for a few seconds. Samples were then studied under TEM without further sample preparations. This collection method ensured the purity and cleanliness of the collected nanoparticles.

Profilometer: The thickness of samples were measured with a KLA Tencor MicroXAM-800.

Supporting Information

Supporting Information is available from the Wiley Online Library or from the author.

Acknowledgements

This material is based upon work supported by the U.S. National Science Foundation (NSF) under grant No. 1923363. SEM imaging was conducted at the National Center for Additive Manufacturing Excellence (NCAME) at Auburn University. Alabama Micro/Nanoelectronic Science and Technology Center (AMNSTC) at Auburn University provided access to the cleanroom facility. STEM characterization was conducted at the Center for Nanophase Materials Sciences (CNMS), which is a DOE Office of Science User Facility.

Conflict of Interest

The authors declare no conflict of interest.

Author Contributions

Z.A. designed and performed the experimental setup, synthesis and processing experiments, materials characterization, data analysis, and manuscript writing. S.L. participated in the SEM imaging and analysis experiments. R.R.U. participated in STEM imaging and analysis experiments. N.S. participated in experimental design, data analysis, and discussions. M.M.S. led the project, experimental design, data acquisition and analysis, discussions, and manuscript preparation. All the authors participated in manuscript preparation and revision processes.

Data Availability Statement

Data available on request from the authors.

Keywords

additive nanomanufacturing, direct writing, dry printing, laser-based printing, multifunctional materials, patterning

Received: December 17, 2020
Revised: January 31, 2021
Published online: March 26, 2021

© 2021 Wiley-VCH GmbH

[1] J. Jiang, *J. Cleaner Prod.* **2020**, *272*, 122916.
[2] N. Li, S. Huang, G. Zhang, R. Qin, W. Liu, H. Xiong, G. Shi, J. Blackburn, *J. Mater. Sci. Technol.* **2019**, *35*, 242.
[3] W. E. Frazier, *J. Mater. Eng. Perform.* **2014**, *23*, 1917.
[4] T. D. Ngo, A. Kashani, G. Imbalzano, K. T. Q. Nguyen, D. Hui, *Composites, Part B* **2018**, *143*, 172.
[5] J. Kranz, D. Herzog, C. Emmelmann, *J. Laser Appl.* **2014**, *27*, S14001.
[6] R. Russell, D. Wells, J. Waller, B. Poorganji, E. Ott, T. Nakagawa, H. Sandoval, N. Shamsaei, M. Seifi, in *Additive Manufacturing for the Aerospace Industry*, (Eds: F. Froes, R. Boyer), Elsevier, Amsterdam, Netherlands **2019**, pp. 33–66.
[7] K. S. Prakash, T. Nancharaih, V. V. S. Rao, *Mater. Today* **2018**, *5*, 3873.
[8] S. Lee, Z. Ahmadi, J. W. Pegues, M. Mahjouri-Samani, N. Shamsaei, *Opt. Laser Technol.* **2021**, *134*, 106639.
[9] S. M. Thompson, L. Bian, N. Shamsaei, A. Yadollahi, *Addit. Manuf.* **2015**, *8*, 36.
[10] B. Kumar, B. K. Kaushik, Y. S. Negi, *Polym. Rev.* **2014**, *54*, 33.
[11] M.-s. Hwang, B.-y. Jeong, J. Moon, S.-K. Chun, J. Kim, *Mater. Sci. Eng., B* **2011**, *176*, 1128.
[12] S. K. Karunakaran, G. M. Arumugam, W. Yang, S. Ge, S. N. Khan, X. Lin, G. Yang, *J. Mater. Chem. A* **2019**, *7*, 13873.
[13] H.-R. Lim, H. S. Kim, R. Qazi, Y.-T. Kwon, J.-W. Jeong, W.-H. Yeo, *Adv. Mater.* **2020**, *32*, 1901924.
[14] W. Su, B. S. Cook, Y. Fang, M. M. Tentzeris, *Sci. Rep.* **2016**, *6*, 35111.
[15] S. Maruo, K. Ikuta, H. Korogi, *Appl. Phys. Lett.* **2002**, *82*, 133.
[16] A. Rashti, B. Wang, E. Hassani, F. Feyzbar-Khalkhali-Nejad, X. Zhang, T.-S. Oh, *Energy Fuels* **2020**, *34*, 6448.
[17] M. Rafiee, R. D. Farahani, D. Therriault, *Adv. Sci.* **2020**, *7*, 1902307.
[18] T. Seifert, E. Sowade, F. Roscher, M. Wiemer, T. Gessner, R. R. Baumann, *Ind. Eng. Chem. Res.* **2015**, *54*, 769.
[19] L. Nayak, S. Mohanty, S. K. Nayak, A. Ramadoss, *J. Mater. Chem. C* **2019**, *7*, 8771.
[20] M. Singh, H. M. Haverinen, P. Dhagat, G. E. Jabbour, *Adv. Mater.* **2010**, *22*, 673.
[21] Y. Khan, A. Thielens, S. Muin, J. Ting, C. Baumbauer, A. C. Arias, *Adv. Mater.* **2020**, *32*, 1905279.
[22] H. Li, J. Liang, *Adv. Mater.* **2020**, *32*, 1805864.
[23] N. J. Wilkinson, M. A. A. Smith, R. W. Kay, R. A. Harris, *Int. J. Adv. Manuf. Technol.* **2019**, *105*, 4599.
[24] S. Lu, J. A. Cardenas, R. Worsley, N. X. Williams, J. B. Andrews, C. Casiraghi, A. D. Franklin, *ACS Nano* **2019**, *13*, 11263.
[25] Y. Chu, C. Qian, P. Chahal, C. Cao, *Adv. Sci.* **2019**, *6*, 1801653.
[26] C. Zhang, L. McKeon, M. P. Kremer, S.-H. Park, O. Ronan, A. Seral-Ascaso, S. Barwich, C. Ó. Coileáin, N. McEvoy, H. C. Nerl, B. Anasori, J. N. Coleman, Y. Gogotsi, V. Nicolosi, *Nat. Commun.* **2019**, *10*, 1795.
[27] D. W. Yee, M. L. Lifson, B. W. Edwards, J. R. Greer, *Adv. Mater.* **2019**, *31*, 1901345.
[28] M. Alssabbagh, A. A. Tajuddin, M. Abdulmanap, R. Zainon, *Radiat. Phys. Chem.* **2017**, *135*, 106.
[29] S. Bodkhe, P. Ermanni, *Eur. Polym. J.* **2020**, *132*, 109738.
[30] A. Nadernezhad, N. Khani, G. A. Skvortsov, B. Toprakhisar, E. Bakirci, Y. Menceloglu, S. Unal, B. Koc, *Sci. Rep.* **2016**, *6*, 33178.
[31] R. Gheisari, H. Chamberlain, G. Chi-Tangyie, S. Zhang, A. Goulas, C.-K. Lee, T. Whittaker, D. Wang, A. Ketharam, A. Ghosh, B. Vaidhyanathan, W. Whittow, D. Cadman, Y. C. Vardaxoglou, I. M. Reaney, D. S. Engstrøm, *Virtual Phys. Prototyping* **2020**, *15*, 133.
[32] E. B. Joyee, Y. Pan, *J. Manuf. Processes* **2020**, *56*, 1178.
[33] D. Han, H. Lee, *Curr. Opin. Chem. Eng.* **2020**, *28*, 158.
[34] V. G. Rocha, E. Saiz, I. S. Tirichenko, E. García-Tuñón, *J. Mater. Chem. A* **2020**, *8*, 15646.
[35] R. D. Farahani, M. Dubé, D. Therriault, *Adv. Mater.* **2016**, *28*, 5794.
[36] W. Y. Padrón-Hernández, M. C. Ceballos-Chuc, D. Pourjafari, G. Oskam, J. C. Tinoco, A. G. Martínez-López, G. Rodríguez-Gattorno, *Mater. Sci. Semicond. Process.* **2018**, *81*, 75.
[37] A. J. Huckaba, Y. Lee, R. Xia, S. Paek, V. C. Bassetto, E. Oveisi, A. Lesch, S. Kinge, P. J. Dyson, H. Girault, M. K. Nazeeruddin, *Energy Technol.* **2019**, *7*, 317.
[38] D. Friedmann, A. F. Lee, K. Wilson, R. Jalili, R. A. Caruso, *J. Mater. Chem. A* **2019**, *7*, 10858.
[39] M. Mahjouri-Samani, M. Tian, A. A. Puretzky, M. Chi, K. Wang, G. Duscher, C. M. Rouleau, G. Eres, M. Yoon, J. Lasseter, K. Xiao, D. B. Geohegan, *Nano Lett.* **2017**, *17*, 4624.
[40] M. Tian, M. Mahjouri-Samani, K. Wang, A. A. Puretzky, D. B. Geohegan, W. D. Tennyson, N. Cross, C. M. Rouleau, T. A. Zawodzinski, G. Duscher, G. Eres, *ACS Appl. Mater. Interfaces* **2017**, *9*, 22018.
[41] P. Fathi-Hafshejani, H. Johnson, Z. Ahmadi, M. Roach, N. Shamsaei, M. Mahjouri-Samani, *ACS Omega* **2020**, *5*, 16744.
[42] B. Yang, M. Mahjouri-Samani, C. M. Rouleau, D. B. Geohegan, K. Xiao, *Phys. Chem. Chem. Phys.* **2016**, *18*, 27067.
[43] C. Polley, T. Distler, R. Detsch, H. Lund, A. Springer, A. R. Boccaccini, H. Seitz, *Materials* **2020**, *13*, 1773.
[44] S. M. Gaytan, M. A. Cadena, H. Karim, D. Delfin, Y. Lin, D. Espalin, E. MacDonald, R. B. Wicker, *Ceram. Int.* **2015**, *41*, 6610.
[45] M. Mikolajek, T. Reinheimer, N. Bohn, C. Kohler, M. J. Hoffmann, J. R. Binder, *Sci. Rep.* **2019**, *9*, 13324.
[46] E. Gilshtein, S. Bolat, G. T. Sevilla, A. Cabas-Vidani, F. Clemens, T. Graule, A. N. Tiwari, Y. E. Romanyuk, *Adv. Mater. Technol.* **2020**, *5*, 2000369.
[47] D. S. Engstrom, B. Porter, M. Pacios, H. Bhaskaran, *J. Mater. Res.* **2014**, *29*, 1792.
[48] C. Zhao, P. J. Shah, L. J. Bissell, *Nanoscale* **2019**, *11*, 16187.
[49] M. S. Alam, Q. Zhan, C. Zhao, *Nano Lett.* **2020**, *20*, 5057.
[50] W. Xiong, Y. S. Zhou, X. N. He, Y. Gao, M. Mahjouri-Samani, L. Jiang, T. Baldacchini, Y. F. Lu, *Light: Sci. Appl.* **2012**, *1*, e6.
[51] Z. Zhang, J. Yan, T. Kuriyagawa, *Int. J. Extreme Manuf.* **2019**, *1*, 022001.
[52] K. Sugioka, *Int. J. Extreme Manuf.* **2019**, *1*, 012003.
[53] F. Fang, N. Zhang, D. Guo, K. Ehmann, B. Cheung, K. Liu, K. Yamamura, *Int. J. Extreme Manuf.* **2019**, *1*, 012001.
[54] Z. Ahmadi, B. Yakupoglu, N. Azam, S. Elafandi, M. Mahjouri-Samani, *Int. J. Extreme Manuf.* **2019**, *1*, 015001.
[55] Z. Ahmadi, B. Yakupoglu, N. Azam, S. Elafandi, M. Mahjouri-Samani, *J. Laser Appl.* **2019**, *31*, 031202.
[56] M. Izadi, A. Farzaneh, M. Mohammed, I. Gibson, B. Rolfe, *Rapid Prototyping J.* **2020**, *26*, 1059.
[57] N. Shamsaei, A. Yadollahi, L. Bian, S. M. Thompson, *Addit. Manuf.* **2015**, *8*, 12.
[58] O. Frank, M. Zukalova, B. Laskova, J. Kürti, J. Koltai, L. Kavan, *Phys. Chem. Chem. Phys.* **2012**, *14*, 14567.
[59] K. F. McCarty, *Appl. Opt.* **1987**, *26*, 4482.
[60] A. Hu, R. Li, D. Bridges, W. Zhou, S. Bai, D. Ma, P. Peng, *J. Laser Appl.* **2016**, *28*, 022602.
[61] W. Qiao, W. Huang, Y. Liu, X. Li, L.-S. Chen, J.-X. Tang, *Adv. Mater.* **2016**, *28*, 10353.
[62] Z. Ahmadi, P. Fathi-Hafshejani, E. Kayali, M. Beidaghi, M. Mahjouri-Samani, *Nanotechnology* **2020**, *32*, 055302.

© 2021 Wiley-VCH GmbH